Force Transmission in Cohesive Granular Media

Farhang Radjai, Vincent Topin, Vincent Richefeu, Charles Voivret, Jean-Yves Delenne, Emilien Azéma, Moulay Saïd El Youssoufi

Force transmission in cohesive granular media

Farhang Radjai[*,†], Vincent Topin[*,†], Vincent Richefeu[**], Charles Voivret[‡], Jean-Yves Delenne[*,†], Emilien Azéma[*] and Said El Youssoufi[*]

[*]*Laboratoire de Mécanique et Génie Civil, UMR 5508 CNRS-Université Montpellier 2, case 048, Pl. E. Bataillon, F-34095 Montpellier cedex 5, France*
[†]*Laboratoire de Micromécanique et Intégrité des Structures, IRSN DPAM-CNRS, case 048, Pl. E. Bataillon, F-34095 Montpellier cedex 5, France*
[**]*Laboratoire Sols Solides Structures Risques, Université Joseph Fourier, Domaine Universitaire, B.P. 53, F-38041 Grenoble, Cedex 9, France.*
[‡]*Laboratoire Surface du Verre et Interfaces, UMR 125 CNRS/Saint-Gobain, 39 Quai Lucien Lefranc, F-93303 Aubervilliers Cedex, France*

Abstract.
We use numerical simulations to investigate force and stress transmission in cohesive granular media covering a wide class of materials encountered in nature and industrial processing. The cohesion results either from capillary bridges between particles or from the presence of a solid binding matrix filling fully or partially the interstitial space. The liquid bonding is treated by implementing a capillary force law within a debonding distance between particles and simulated by the discrete element method. The solid binding matrix is treated by means of the Lattice Element Method (LEM) based on a lattice-type discretization of the particles and matrix. Our data indicate that the exponential fall-off of strong compressive forces is a generic feature of both cohesive and noncohesive granular media both for liquid and solid bonding. The tensile forces exhibit a similar decreasing exponential distribution, suggesting that this form basically reflects granular disorder. This is consistent with the finding that not only the contact forces but also the stress components in the bulk of the particles and matrix, accessible from LEM simulations in the case of solid bonding, show an exponential fall-off. We also find that the distribution of weak compressive forces is sensitive to packing anisotropy, particle shape and particle size distribution. In the case of wet packings, we analyze the self-equilibrated forces induced by liquid bonds and show that the positive and negative particle pressures form a bi-percolating structure.

Keywords: granular media, force chain, granular disorder, cohesion, discrete element method, lattice element method, capillary bond, binding matrix
PACS: 45.70.-n, 81.05.Rm, 61.43.Hv

INTRODUCTION

A considerable amount of experimental and numerical work has been devoted to force transmission in model granular media such as glass bead packs [1, 2, 3, 4, 5, 6]. The force transmission in granular materials is essential for microscopic modeling of constitutive behavior and for many industrial processes that involve a better understanding of the static or dynamic forces experienced by the particles. The force distributions are found to be broad and highly heterogeneous. This heterogeneity is often described in terms of *force chains* and linked with the concept of *jamming*.

The issue that we would like to address in this paper, is to which extent the well-known features of force distributions in noncohesive granular media apply to cohesive granular media. The latter covers a wide class of materials encountered in nature and industry. Well-known examples are sedimentary rocks, wet soils, and fine and sintered powders. In contrast to noncohesive granular media, all these materials are endowed with *cohesion* resulting either from direct surface forces between particles or from the presence of a binding phase filling fully or partially the interstitial space. The effect of surface forces or a binder is to freeze or restrict the relative degrees of freedom (separation, sliding, rolling) between particles up to a threshold. Hence, depending on the boundary conditions, tensile forces can develop in cohesive granular media and their distributions are dictated by the conditions of force balance and granular disorder as in the case of compressive forces. Obviously, the distribution of tensile forces is of particular relevance to the stress intensity factor which controls the initiation and propagation of cracks.

In this paper, we investigate force and stress distributions in granular media involving either liquid bridges or a solid binding matrix between particles. The presence of liquid bridges will be treated by implementing a capillary force law within a debonding distance between particles. The simulations are performed by means of the Discrete Element

Method (DEM) using Molecular Dynamics (MD) and Contact Dynamics approaches. For solid binding, we adopt a broad framework allowing for the numerical treatment of a binding matrix with variable volume fraction. The effect of small amounts of the matrix localized at the contact zones between particles can be assimilated to that of a surface force. The force transmission in this limit is correlated with the packing structure. The other limit of high matrix volume fractions corresponds to a *cemented* granular material in which the particles are fully or partially embedded in the binding matrix. The force transmission is thus mediated both by the particles and matrix and governed by the details of the composition (phase volume fractions) and the material properties of each phase (relative stiffness, particle-matrix interface adherence).

The treatment of the matrix, as a continuous phase, requires a numerical method capable of resolving the matrix. We use the Lattice Element Method (LEM) which is found to be numerically efficient. It is based on a lattice-type discretization of all phases including the particles, matrix and their interface [7, 8, 9]. The elastic deformations of the particles are taken into account not only at their contacts with other particles or with the matrix, as in the DEM, but also in their bulk. The matrix can be introduced with the desired volume at the contact zones between the particles and in the pores with its elastic properties and adhesion with the particles. An advantage of the LEM is to give us access to stresses in the bulk of the particles and binding matrix. Hence, the forces at the contact zones can be estimated by coarse-graining from the stresses and compared to the DEM predictions for the same granular configuration.

In the following, we first focus on some important features of force transmission in noncohesive granular media. We consider both 2D and 3D granular samples and the effect of particle shape and size distribution. One section is devoted to granular media with solid bridging. The LEM is briefly introduced together with numerical procedures for sample preparation. Our main numerical results will be presented by considering the force distributions in 2D packings simulated alternatively by LEM and DEM in the limit of low matrix volume fractions, the stresses in a 3D packing and the effect of matrix volume fraction, particle stiffness and particle volume fraction on stress distributions. In another section we consider liquid bridging. We first introduce the capillary force law implemented in MD simulations. Then, we analyze the force distributions with and without a confining pressure. We also consider the tensile and compressive stresses supported by the particles. We conclude the paper with a summary of the most salient features of force transmission in cohesive granular media.

FORCE DISTRIBUTIONS IN NONCOHESIVE GRANULAR MEDIA

We study in this section the normal force distributions from numerical simulations by CD and MD methods in 2D and 3D. We consider the effect of packing anisotropy, particle shape and particle size distribution (PSD). Some of these features will be revisited in the next sections in the presence of liquid or solid binding between particles.

Background

Granular disorder and steric exclusions lead to an unexpectedly inhomogeneous distribution of contact forces under quasistatic loading [1, 10, 3, 11, 5, 12, 13, 14, 15, 6]. These force inhomogeneities in granular assemblies were first observed by means of photoelastic experiments [16, 17]. The carbon paper technique was used later to record the force prints at the boundaries of a granular packing [3]. It was found that the forces have a nearly decreasing exponential distribution. Numerical simulations by the contact dynamics (CD) method provided detailed evidence for force chains, the organization of the force network into strong and weak networks, and the exponential distribution of strong forces [18, 4]. Moreover, the force probability density functions (PDF's) from simulations showed that the weak forces (below the average force) in a sheared granular system have a nearly uniform or decreasing power law shape in agreement with refined carbon paper experiments [10, 5].

Further experiments and numerical simulations have shown that the exponential falloff of strong forces is a robust feature of force distribution in granular media both in two and three dimensions. In contrast, the weak forces are sensitive to the details of the preparation method or the internal state of the packing [19, 20, 15, 6]. A remarkable aspect of weak forces is the fact that their number does not vanish as the force falls to zero [18, 21]. Several theoretical models have been proposed allowing to relate the exponential distribution of forces to granular disorder combined with the condition of force balance for each particle [1, 22]. Recently, the force PDF's were derived for an isotropic system of frictionless particles in two dimensions from a statistical approach assuming a first shell approximation (one particle with its contact neighbors) [21].

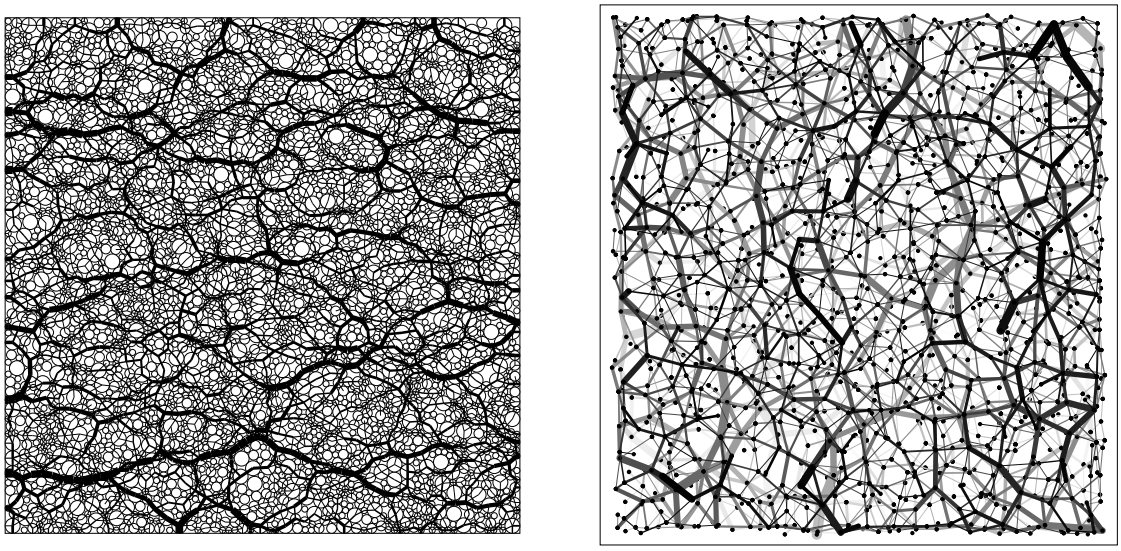

(a) (b)

FIGURE 1. The force network in a 2D packing of disks (a) and in a thin layer cut inside a 3D packing of spherical particles (b). The line thickness is proportional to the normal force. The gray level in the 3D system represents the field depth.

Figure 1 displays a 2D packing simulated by the CD method. The normal forces are encoded as the thickness of branch vectors (joining particle centers). In the same figure, the force network in a thin layer for a 3D packing of spherical particles subjected to axial compression is shown. Strong force chains are easily distinguished in both cases. The strongest chains have a linear aspect and they are mostly parallel to the axis of compression (vertical).

Discrete Element Method

The Discrete Element Method (DEM) has been extensively used since the pioneering work of Cundall for the simulation of granular materials [23]. In this method, the equations of motion are integrated for all particles by taking into account their contact interactions. In its original version, commonly used also today, the particles are treated as rigid elements but the interactions are modeled by means of visco-elastic force laws expressed in terms of the relative displacements between particles as in classical Molecular Dynamics (MD) simulations. In these MD-type approaches, the simulation of mutual exclusions between particles requires a stiff repulsive potential and thus high time resolution. In the same way, the Coulomb law for dry friction needs to be regularized such that the friction force can be expressed as a (mono-valued) function of relative tangential displacement.

The Contact Dynamics (CD) method, introduced later, provides an alternative approach based on *nonsmooth* formulation of mutual exclusion and dry friction between particles [24, 25, 26]. In this method, the equations of motion are expressed as differential inclusions and the accelerations are replaced by velocity jumps. At each time step, all kinematic constraints implied by enduring contacts and possible rolling of particles over one another are simultaneously taken into account in order to determine all velocities and contact forces. In the generic CD algorithm, an iterative process is used to solve this problem. It consists of solving a single contact problem with all other contact forces kept constant, and iteratively updating the forces until a given convergence criterion is fulfilled. Due to the implicit time integration scheme inherent in the CD method, the solution is unconditionally stable. The particle positions are updated from the calculated particle velocities before a new detection of the contacts between particles is performed.

Schematically, the MD method is based on a description of particle interactions in terms of *force laws*, i.e. bijective force-displacement relations, whereas the CD method is based on a formulation of kinematic constraints in terms of *contact laws*. Independently of particle deformability, the impenetrability of the particles and the Coulomb friction at the contact zones can be formulated in the form of contact laws expressing the contact actions as set-valued functions of particle positions. The uniqueness of the solution is not guaranteed by CD approach for perfectly rigid particles in

absolute terms. However, by initializing each step of calculation with the forces calculated in the preceding step, the set of admissible solutions shrinks to a small variability basically of the same order of magnitude as the numerical resolution. In the MD method this 'force history' is by definition encoded in the particle positions.

Since the CD method handles the kinematic constraints without resorting to force laws, the particles are often treated as perfectly rigid although finite stiffness can be introduced in the same framework. This is the case of the CD simulations carried out for the analysis of force distributions in this paper. Hence, the only material parameter of the simulated static packings by the CD method is the coefficient of friction μ between the particles. On the other hand, the MD-generated packings are characterized by normal and tangential stiffnesses k_n and k_t as well as the coefficient of friction μ. The mean deformation of the particles is given by the ratio p/k_n of the average stress p to k_n.

Normal force distributions

Different numerical packings were prepared by isotropic compaction and then deformed under either slow triaxial loading in 3D or in simple shear in 2D. The particle inertia are negligibly small compared to the static confining pressure so that the packings can be considered in a *quasi-static state*. As we shall see below, the general shape of force distributions is robust with respect to the details of preparation or the microstructure. But the distribution parameters do depend on the preparation. In all examples considered below the packings are sheared until a steady or *critical* state, in the sense of soil mechanics, is reached. In this state, the shear deformation is isochoric on the average, and the memory of the preparation process is erased as a result of shearing so that the microstructure is a function only of the material parameters. The force distributions will be analyzed either in the initial isotropic state prepared by isotropic compaction with zero coefficient of friction or in the critical state.

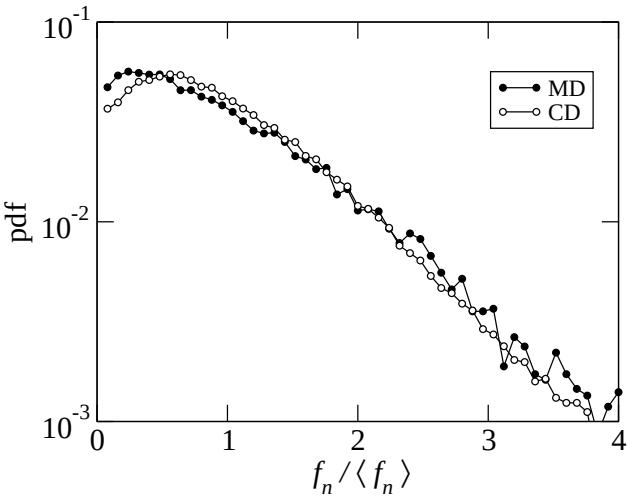

FIGURE 2. Probability density functions of normal forces in two isotropic samples of spherical particles simulated by MD and CD methods.

Figure 2 shows the PDF's of normal forces for two isotropic samples of spherical particles simulated by MD (8000 particles) and CD (20000 particles) methods. The PSD is not the same in the samples but they represent rather weakly polydisperse distributions with a ratio of 2 between the largest and smallest particle diameters. The coefficient of friction is $\mu = 0.4$ between particles and 0 with the walls. The forces have been normalized by the average force in each sample. Although the two samples are not exactly identical, the two PDF's have the same shape characterized by an exponential falloff for large forces, a small peak for a force slightly below the average force and a finite value at zero force. The position of the peak is not the same in the two distributions but the exponents of the exponential falloff are the same within statistical precision of the data:

$$P(f_n) \propto e^{-\beta f_n/\langle f_n \rangle}, \tag{1}$$

with $\beta \simeq 1.4$. This similarity between the two distributions indicates that the statics of a granular system is statistically robust with respect to the numerical approach and, in particular, the small elastic deformation at contact points in MD simulations has negligible effect on the force inhomogeneity. In other words, the physics of a static granular packing

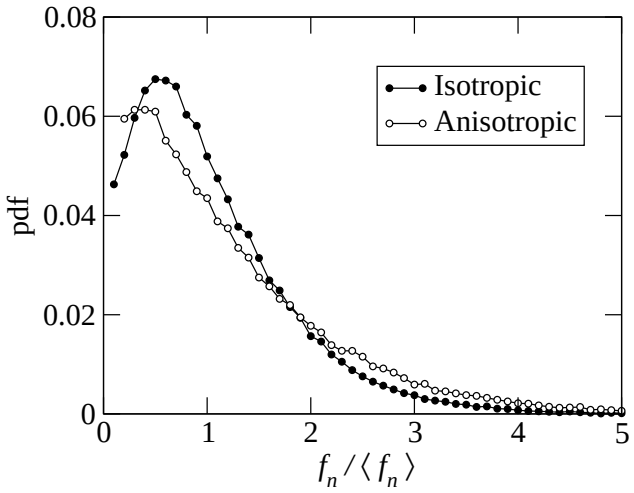

FIGURE 3. Probability density functions of normal forces in a sample of spherical particles after isotropic compaction (isotropic state) and following triaxial compression (anisotropic state).

can be approximated by considering undeformable particles as in the CD method as far as the the ratio p/k_n of the confining pressure p to the normal stiffness k_n of the particles is small (here $\simeq 10^3$).

The observed shape of force PDF's is unique in two respects: (1) the exponential part reflects the presence of very strong forces in the system often appearing in a correlated manner in the form of force chains; (2) the nonvanishing class of weak forces, with a fraction of more than 60% of contact forces below the average force, means that the stability of force chains is ensured by a large number of vanishingly small forces [4, 19]. This is a signature of the *arching effect*. Hence, the average force is a physically poor representative of the broad spectrum of forces in a granular system.

Figure 3 displays the normal force PDF's in CD simulations for the same system of spherical particles both at the isotropic state and at the critical state where the fabric and force chains are anisotropic. The effect of anisotropy is to reinforce the force inhomogeneity by increasing the relative density of weak forces [20, 27, 28]. The exponent

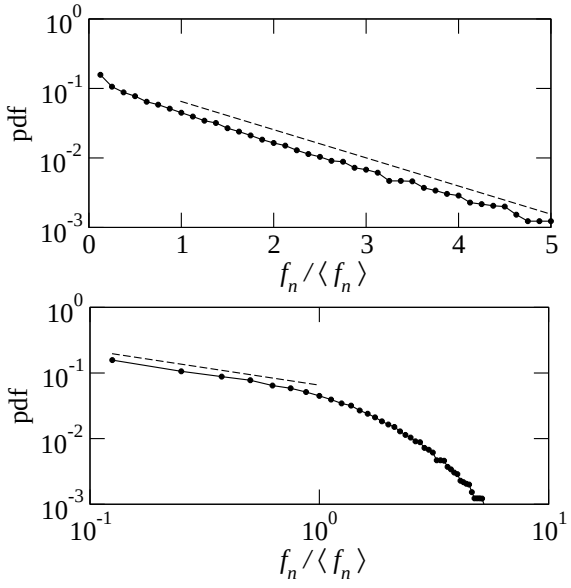

FIGURE 4. Probability density function of normal forces in an isotropic sample of irregular polyhedral particles on log-linear and log-log scales.

β remains nearly unchanged whereas the small peak near the average force disappears and the distribution of weak forces tends to become nearly uniform.

Effect of particle shape

The force distributions are sensitive to particle shapes. Fig. 4 shows the distribution of normal forces in an isotropic 3D sample of 20000 irregular polyhedral particles with $\mu = 0.5$ simulated by the CD method. We again observe the exponential tail of strong forces together with a decreasing power law distribution for weak forces.

The angular particle shape increases considerably the number of very weak forces by enhancing the arching effect. The latter is also reflected in the value of the exponent β reduced to 0.97 compared to 1.4 for spherical particles. In other words, the force chains are stronger but less in number. A detailed analysis of force and fabric anisotropies in this packing reveals the special role of face-to-face contacts in enhancing force anisotropy and thus the overall shear strength as compared to packings of spherical particles [29]. Similar trends are observed in packings of polygonal particles (in 2D simulations) [30].

Effect of particle size distribution

Figure 5 shows the normal force PDF's for increasingly broader particle size span s in a 2D sheared packing of 10000 circular particles simulated by the CD method [31]. The size span is defined by $s = (d_{max} - d_{min})/(d_{max} + d_{min})$ where d_{min} and d_{max} are the smallest and largest diameters, respectively. A monodisperse distribution corresponds to $s = 0$ and the limit $s \simeq 1$ corresponds to an infinitely polydisperse system [32]. The PSD is uniform by particle volume fractions.

The PDF becomes broader with increasing s. The weak forces have a clear power law behavior with increasing exponent α whereas the strong forces fall off exponentially with a decreasing exponent β. The power-law behavior of strong forces can be attributed to a "cascade" mechanism from the largest particles "capturing" strongest force chains down to smaller forces carried by smaller particles [31]. A map of normal forces in a highly polydisperse packing ($s = 0.96$) is shown in Fig. 6. A large number of rattlers, i.e. particles not engaged in the force network, can be observed. Although these particles represent a small volume fraction of the sample, their absence from the force-bearing network contributes to force inhomogeneity.

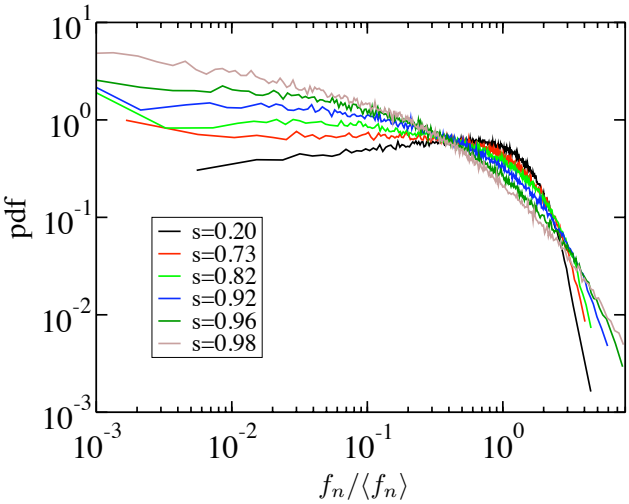

FIGURE 5. Probability density functions of normal forces for increasing span s of particle diameters.

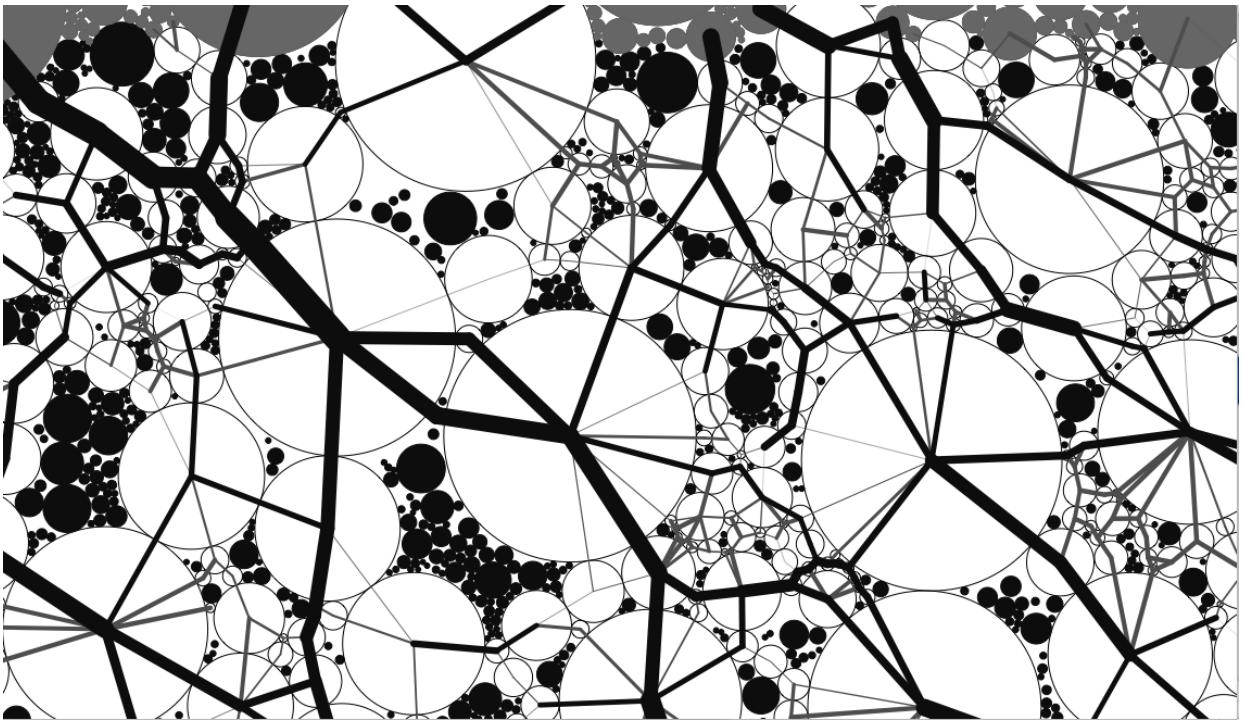

FIGURE 6. A map of normal forces in a highly polydisperse system with a uniform size distribution by particle volume fractions. The black particles are “rattlers" excluded from the force-bearing network.

A generic functional form

The above examples point to a generic PDF of normal forces in a granular packing that can be approximated by the following form [19]:

$$P(f_n) = \begin{cases} A \left(\frac{f_n}{\langle f_n \rangle}\right)^{-\alpha} & f_n/\langle f_n \rangle < 1 \\ A\, e^{\beta(1-f_n/\langle f_n \rangle)} & f_n/\langle f_n \rangle > 1 \end{cases} \tag{2}$$

where A is the normalization factor given by

$$\frac{1}{A} = \frac{1}{1-\alpha} + \frac{1}{\beta} \tag{3}$$

Considering the mean force $\langle f_n \rangle$ as the point of cross-over between the two parts of the distribution, we get the following relation between the exponents:

$$\beta^2 = (1-\alpha)(2-\alpha) \tag{4}$$

Note that the nearly uniform distribution of static forces in the case of sheared circular particles is recovered by setting $\alpha = 0$ in equation (2). Then, from equation [4] we get $\beta = \sqrt{2} \simeq 1.4$ which is the value found for the distribution of forces in sheared packings of weakly polydisperse spheres. For this system, the following fitting form was also proposed by Mueth et al. [5]:

$$P(f) = a\,(1 - be^{-f^2})e^{-\beta f} \tag{5}$$

where $f = f_n/\langle f_n \rangle$. As argued by Mueth et al., the above function for the range of weak forces provides a fit essentially indistinguishable from a power law $f_n^{-\alpha}$ as long as α is positive and close to zero [5].

SOLID BONDING

In this section, we consider cemented granular media in which the local cohesion is a consequence of the presence of a binding phase between the particles.

Numerical method and sample preparation

The LEM is based on a discretization of the phases on a regular or irregular lattice. Hence, the space is represented by a grid of points (nodes) interconnected by one-dimensional elements (bonds). Each bond can transfer normal force, shear force and bending moment up to a threshold in force or energy, representing the cohesion of the phase or its interface with another phase. Each phase (particle, matrix) and its boundaries are materialized by the bonds sharing the same properties. The samples are deformed by imposing displacements or forces to the nodes belonging to the contour. The total elastic energy of the system is a convex function of node displacements and thus finding the unique equilibrium configuration of the nodes amounts to a minimization problem. Performing this minimization for stepwise loading corresponds to subjecting the system to a quasistatic deformation process. The details of this method can be found in Ref. [8].

The samples are constructed either by geometric methods or by isotropic compaction of disk-like particles by DEM simulations by setting the friction coefficient between the particles to zero in order to get a dense packing. The samples are then discretized on a lattice. The matrix is introduced in the form of bridges of variable thickness, depending on the overall matrix volume fraction and the particle sizes, between neighboring particles throughout the system; see Fig. 7. As the matrix volume fraction is increased, the thickness of the bridges increases and eventually they merge to fill the interstitial space.

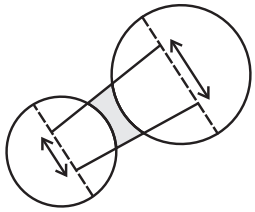

FIGURE 7. Numerical model of cementing bridge between particles. The width is increased for all pairs in a sample until the required matrix volume fraction is reached.

The elastic properties of each phase are controlled by the linear elastic properties of the bonds. The main elastic parameters that will be considered here are the Hooke constants k^p and k^m of the bonds belonging to the particles and matrix, respectively. The initial state is the reference (unstressed) configuration. When the sample is loaded, bond forces develop inside the sample. A stress tensor σ^a can be attributed to each node a of the lattice network: $\sigma^a_{ij} = \frac{1}{V^a} \sum_b r^{ab}_i f^{ab}_j$ where the summation runs over all neighboring nodes j, r^{ab}_i is the i component of the vector joining the node a to the midpoint of the bond ab and f^{ab}_j is the j component of the bond force [33, 8].

The resolution of the stresses depends on the particle size compared to the lattice element lengths. The discretization should be sufficiently fine for the particle contours to be correctly represented. The macroscopic elastic moduli might crucially depend on the discretization as more generally in porous materials. In practice, however, the resolution is set as a result of compromise between the necessary number of particles for statistical representativity and total number of nodes accessible to computer simulation. In the simulations reported in this paper, we generally favored high resolution both in 2D and 3D simulations such that the results for stress transmission reliably reflect the configuration of the particle phase.

In the following, we mainly consider node stresses in rectangular and cubic samples subjected to vertical loading with free lateral boundaries. At low matrix volume fractions, for comparison with DEM we will also evaluate the contact forces between particles from bond forces. During loading, the bond forces increase with the applied vertical stress at the boundary. Hence, the mean bond force increases linearly with the external load whereas the bond force PDF's and stresses do not evolve as long as no bond breaks. We focus here only on force distributions in the undamaged samples, i.e. in the purely elastic domain. The damage and fracture properties have been extensively studied elsewhere [8].

Sub-particle stresses and contact forces

In order to obtain fine statistics of node stresses and contact forces between particles, we simulated a large sample of about 5000 particles with a particle volume fraction of $\rho^p \simeq 0.8$. This corresponds to a packing with a dense contact network of coordination number $z = 4$. The particle diameter d varies between d_{min} and $d_{max} = 3d_{min}$ with a uniform

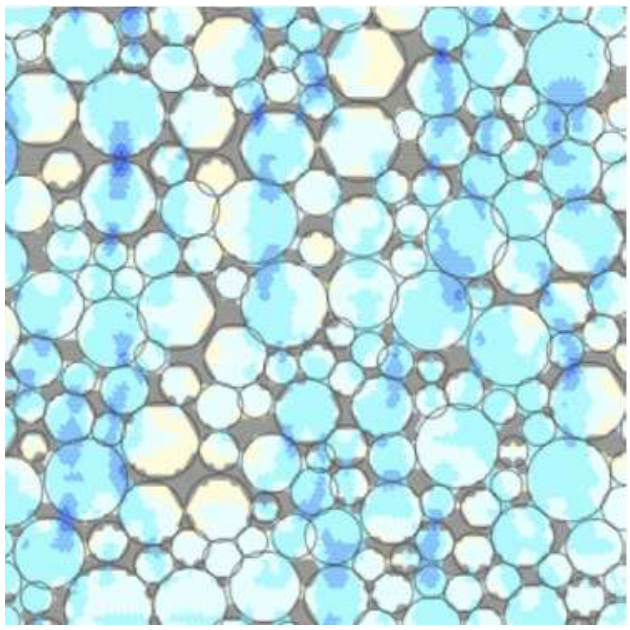

FIGURE 8. Vertical stress field σ_{yy} represented in color level in a cemented packing. The solid bridges and voids are in white and gray, respectively.

distribution by volume fractions ($P(d) \propto d^{-2}$). We would like to compare the contact forces in this system, simulated by the LEM, with those in a similar system simulated by the DEM. This can be done only in the limit of a small matrix volume fraction where the matrix is found in the form of small solid bridges between the particles such that its effect can be represented by a cohesion law. We used a matrix volume fraction of $\rho^m \simeq 0.01$. The DEM code is based on the standard molecular dynamics method with cohesive bonding between the particles. The sample is subjected to vertical compression.

Figure 8 shows the vertical stress field σ_{yy}. The node stresses are represented by proportional color levels over the elementary hexagonal cells centered on each node. We observe chains of highly stressed particles and higher concentration at the contact zones between the particles. In order to compare the LEM simulated packing with DEM simulations of the same packing, for which only contact forces are accessible, we compute the contact forces $\vec{f}$ by summing up the bond forces $\vec{f^{ab}}$ for all bonds ab crossing the contact plane S: $\vec{f} = \sum_{ab \in S} \vec{f^{ab}}$.

Figure 9 shows the map of normal forces between particles for the LEM and DEM packings. We observe very similar force chains despite the fact that radically different methods were used to simulate them. The Pearson product-moment correlation coefficient between the two force networks is $r = 0.92$, which indicates high similarity. The PDF's of normal and tangential forces from LEM and DEM simulations are shown in Fig. 10. We observe that the two PDF's coincide over nearly the whole range of forces. The distribution of normal forces involves an exponential fall-off in the ranges of strong compressive and for the whole range of tensile forces. The exponent in the range of tensile forces is larger than that for the compressive forces. Remark that the largest tensile forces are far below the breaking threshold. The distribution is uniform in the range of weak compressive and forces as also observed in most simulations of sheared packings composed of circular weakly polydisperse particles (see section). This excellent agreement between the force PDF's with $\beta \simeq 1.35$ may be considered as a validation of DEM results for the force networks in the sense that the contact forces in LEM simulations are calculated from a finer scale [2, 5, 6].

Having access to the node stresses, it is interesting to evaluate their PDF's in order to see whether they carry a signature of the composition. One example of the PDF of vertical stresses σ_{yy} is displayed in Fig. 11(a) for a packing under vertical compression. Since the sample is under axial compression, only 4% of vertical stresses are tensile and are thus not shown in Fig. 11(a). Interestingly, the strong stresses fall off exponentially as contact forces (see Fig. 10), $P_\sigma(\sigma_{yy}) \propto e^{-\beta \sigma_{yy}/\langle \sigma_{yy} \rangle}$ with $\beta \simeq 0.95$, and they mostly concentrate at the contact zones. The weak stresses have a nonzero PDF, much the same as weak contact forces, reflecting the arching effect. Since the contact force distributions reflect the granular disorder, i.e. the structure of the network of contiguous particles, the observed

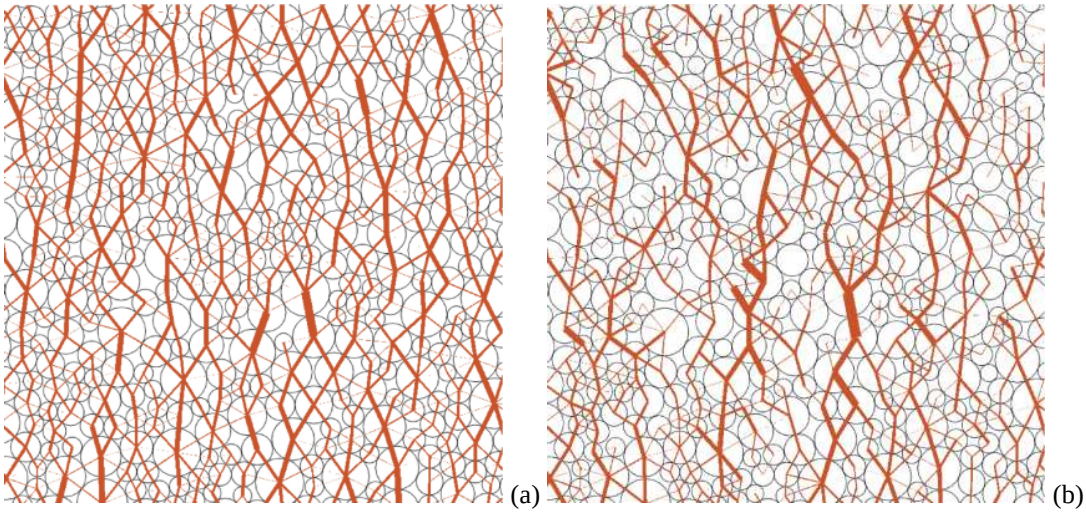

FIGURE 9. A map of normal forces in a portion of a sample under vertical compression simulated by DEM (a) and LEM (b). Line thickness is proportional to the normal force. Very weak and tangential forces are not shown.

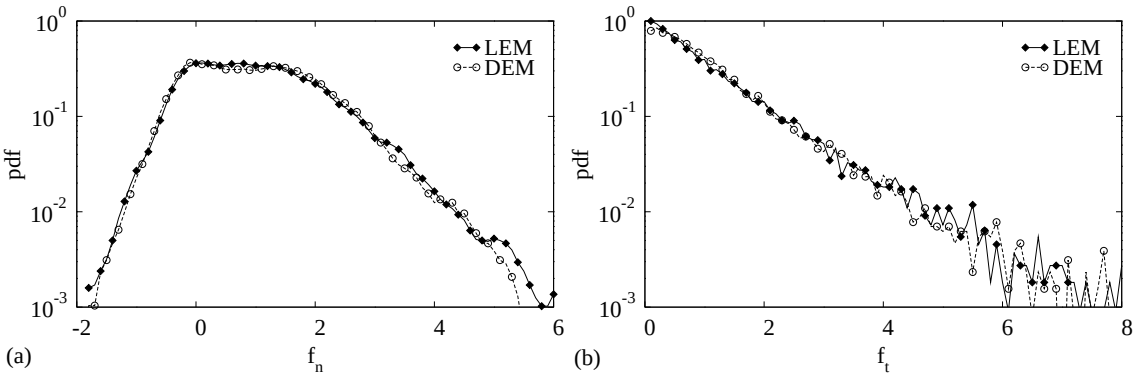

FIGURE 10. Probability density function of normal forces (a) and tangential forces (b) in a sample axially compressed by LEM and DEM simulations. The forces are normalized by the mean normal force.

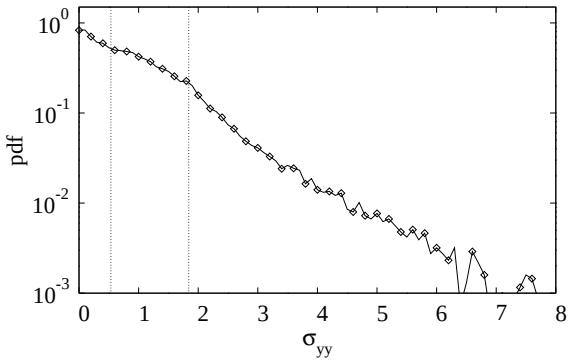

FIGURE 11. Probability density function of vertical stresses normalized by the average stress in compression.

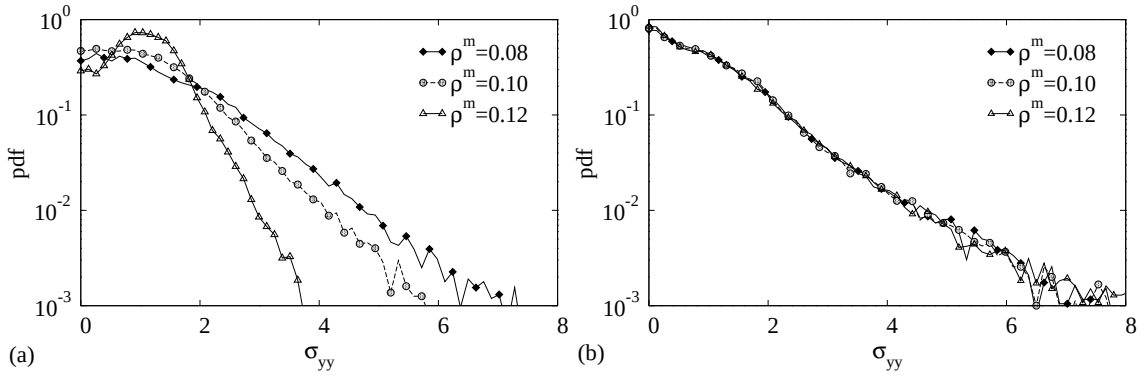

FIGURE 12. Probability density functions of normalized vertical stresses for three values of the matrix volume fraction (a) in tension and (b) in compression.

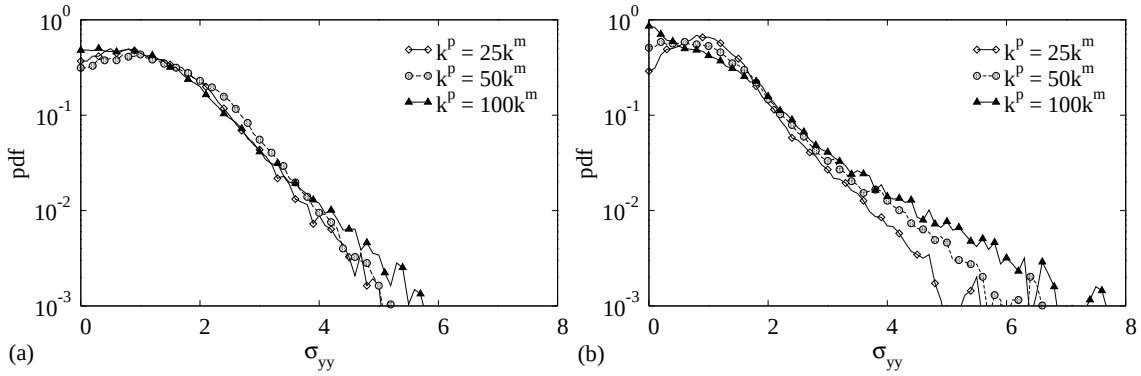

FIGURE 13. Probability density functions of normalized vertical stresses for three values of the relative stiffness k^p/k^m (a) in tension and (b) in compression.

similarity between the distributions of stresses and forces means that the sub-particle stresses are strongly affected by the granular disorder.

Effect of matrix volume fraction

It is expected that at higher matrix contents the stress is more homogeneously redistributed inside the packing due to load transfer between the particles and the matrix. Fig. 12 shows P_σ for three values of ρ^m in tension and compression for $k^p = 100k^m$. Interestingly, the exponential tail persists both in tension and in compression, but for equal matrix volume fractions, the PDF of strong stresses is broader in compression than in tension. In other words, the stress redistribution is more homogeneous in tension than in compression.

It is also interesting to observe that the stress PDF is not affected by the matrix volume fraction in compression but it is increasingly broader in tension for decreasing matrix content so that the stresses are more and more concentrated in the bridges between the particles. In tension, the exponent β varies from 1.10 to 2.55 as ρ^m varies from 0.08 to 0.12 whereas in compression we have $\beta \simeq 0.95$ for all ρ^m. As ρ^m increases, the gaussian peaked on the mean stress, corresponding mainly to the stresses in the bulk of the particles, becomes more and more pronounced.

Particle/matrix stiffness ratio

We now consider the influence of the particle/matrix stiffness ratio k^p/k^m on stress distribution. Fig. 13 displays the vertical stress PDF's for three values of k^p/k^m in tension and compression for $\rho^m = 0.10$. It is remarkable that

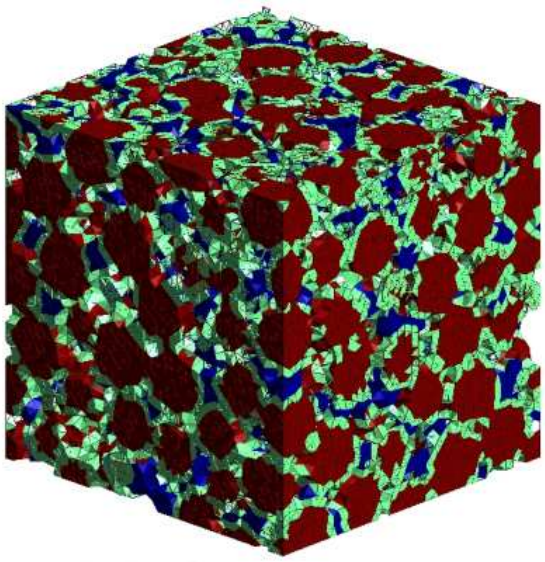

FIGURE 14. (Color online) Representation of a cemented granular sample composed of particles (in red), interfaces (in green) and matrix (in blue) discretized on a 3D irregular lattice.

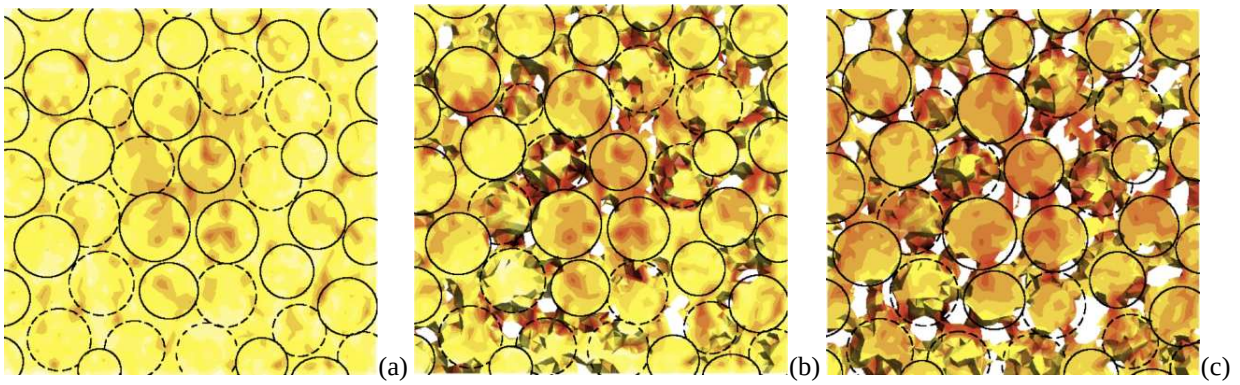

FIGURE 15. (Color on line) Vertical stresses field σ_{yy} in the 3D packing on a cut plane in color level for (a) $\rho^m = 0.37$, (b) $\rho^m = 0.23$, (c) $\rho^m = 0.10$.

in tension the particle stiffness has little influence on the pdf whereas in compression the pdf becomes increasingly broader for an increasing particle stiffness. The respective effects of particle stiffness and matrix volume fraction can be understood by remarking that, due to the presence of a granular backbone, the stress chains are essentially guided by the cementing matrix in tension and by the particle phase in compression. Therefore, the stress transmission is not affected by the matrix volume fraction in compression and only slightly influenced by particle stiffness in tension.

Effect of composition in 3D

We briefly extend here our studies to 3D cemented granular solids. We generated a dense packing of 300 particles discretized over an irregular 3D lattice containing about 500 000 elements. The particle diameters d vary between d_{min} and $d_{max} = 2d_{min}$ with a uniform distribution by volume fractions.The particle volume fraction is $\rho^p \simeq 0.63$. As in our 2D LEM simulations, the matrix is distributed uniformly in the form of bridges of varying thickness and section between neighboring particles. The filling fraction depends on the cross section of the bridges. This protocol allows us to vary the matrix volume fraction continuously from 0 to 0.37. The sample is displayed in Fig. 14.

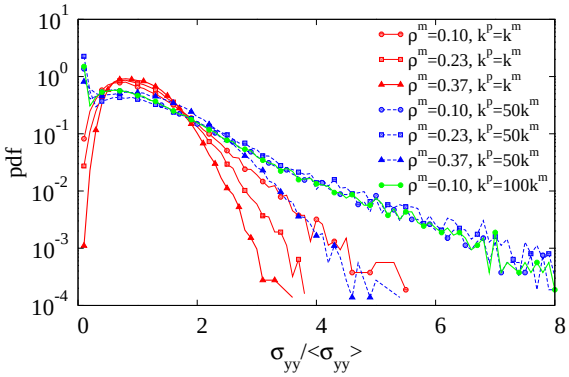

FIGURE 16. Probability density functions of normalized vertical stresses for different values of stiffness ratio k^p/k^m and values of the matrix volume fraction ρ^m in compression.

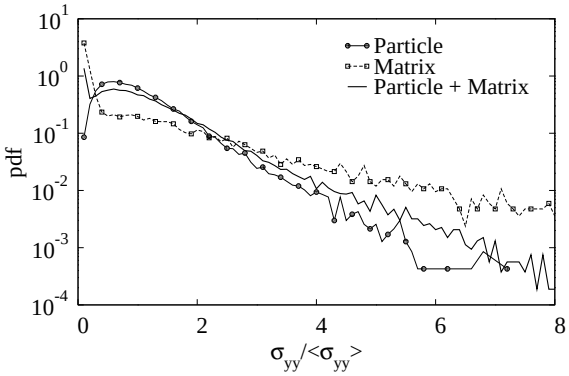

FIGURE 17. Probability density functions of normalized vertical stresses for $\rho^m = 0.1$ and $k^p/k^m = 50$ in the particle and matrix phases in comparison with that in the whole sample.

Fig. 15 displays a map of vertical stresses on a cut plane for three values of ρ^m. We observe that the stresses are more and more localized in the matrix bridges as the matrix volume fraction is reduced. Figure 16 shows the vertical stress pdf's for three values of k^p/k^m and three values of ρ^m under vertical compression with free lateral boundaries. Two limits can be distinguished: (1) The *homogeneous limit* characterized by $\rho^m = 0.37$ and $k^p = k^m$, corresponding to a homogeneous material with no void and no particle (absence of elastic contrast between particles and matrix); (2) The *granular limit* characterized by large k^p and weak amount of matrix (here $\rho^m = 0.1$) basically distributed in the form of small solid bonds between particles. The latter corresponds to a granular material with stiff particles as generally assumed in DEM simulations. We see that, as expected, the stress distribution in the homogeneous limit is the less broad one with a nearly gaussian shape. The stress variability in this system reflects the metric disorder of the underlying lattice. The distribution for $\rho^m = 0.1$ and $k^p/k^m = 100$ corresponds to the granular limit.

The strong stresses have a decreasing exponential distribution as in 2D packings in the granular limit with as exponent increasing with matrix volume fraction. A secondary peak is observed in the range of very weak stresses in all cases where the particles are stiffer than the matrix. This peak reflects the weak stresses inside the matrix bridges, as suggested by Fig. 17 where the distributions are separately plotted for the stresses in the matrix and inside the particles in the case $\rho^m = 0.1$ and $k^p/k^m = 100$. We see that the particles involve no stress peak. This peaks is thus a consequence of the low stiffness of the binding phase.

The distribution in the granular limit is practically the broadest one, and hence all distributions for all parameters lie between those for the granular and homogeneous limits. For $\rho^m = 0.23$ and $k^p/k^m = 1$ we have a porous material with no mechanical contrast between the matrix and particles. For $\rho^m = 0.37$ and $k^p/k^m = 50$ we have a granular phase embedded in a matrix with no voids. In both these cases, the stress distribution is broader than that in the homogeneous limit although the physical origins of this enhanced inhomogeneity are different. We remark that, for $\rho^m = 0.1$, increasing k^p/k^m from 50 to 100 has little influence on the stress distribution. In the same way, for

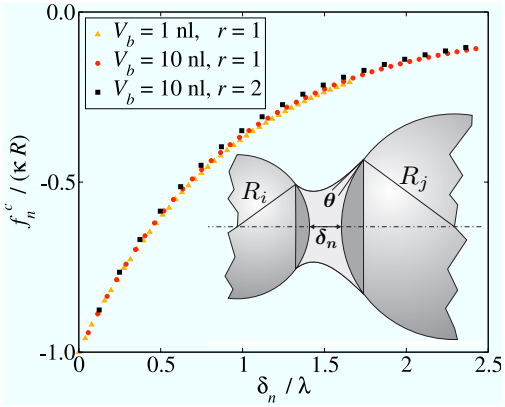

FIGURE 18. Scaled plot of the capillary force as a function of the gap between two particles for different values of the local liquid volume V_b and size ratio r according to the model proposed in this paper. Inset: Geometry of a capillary bridge.

$k^p/k^m = 50$, increasing ρ^m from 0.1 to 0.23 has practically no impact on the distribution.

LIQUID BONDING

In this section, we investigate force transmission in wet granular media composed of rigid particles interconnected by capillary bridges. The action of the capillary bridges is modeled by a capillary force law and implemented in a 3D MD code.

Numerical method

For the simulations of wet granular materials, we used the MD method with spherical particles and a capillary force law. The total normal force f_n at each contact is the sum of a repulsive force f_n^r and an attractive capillary force f_n^c. The latter is a function of the liquid bond parameters, namely the gap δ_n, the liquid bond volume V_b, the liquid surface tension γ_s, and the particle-liquid-gas contact angle θ; see inset in Fig. 18. The capillary force can be calculated by integrating the Laplace-Young equation [34, 35, 36]. However, for efficient MD simulations, we need an explicit expression of f_n^c as a function of the liquid bond parameters.

We used an analytical form for the capillary force which is well fitted by the data from direct integration of the Laplace-Young equation both for polydisperse particles [37]. At leading order, the capillary force f_0 at contact, i.e. for $\delta_n \leq 0$, is

$$f_0 = -\kappa R, \tag{6}$$

where R is a length depending on the particle radii R_i and R_j and κ is given by [38, 39, 40]

$$\kappa = 2\pi\gamma_s \cos\theta. \tag{7}$$

A negative value of δ_n corresponds to an overlap between the particles. The assumption is that the overlap is small compared to the particle diameters. The data obtained from direct integration of the Laplace-Young equation show that the geometric mean $R = \sqrt{R_i R_j}$ is more suited than the harmonic mean $2R_iR_j/(R_i+R_j)$ proposed by Derjaguin for polydisperse particles in the limit of small gaps (see below) [41]. We also note that f_0 in Eq. (6) is independent of the bond liquid volume V_b.

The adhesion force f_0 at contact is the highest level of the capillary force. The latter declines as the gap δ_n increases. The capillary bridge is stable as long as $\delta_n < \delta_n^{max}$, where δ_n^{max} is the debonding distance given by [42]

$$\delta_n^{max} = \left(1 + \frac{\theta}{2}\right) V_b^{1/3}. \tag{8}$$

Between these two limits, the capillary force falls off exponentially with δ_n:

$$f_n^c = f_0 e^{-\delta_n/\lambda}, \tag{9}$$

where λ is a length scale which should be a function of V_b and the particle radii. The asymmetry due to unequal particle sizes is taken into account through a function of the ratio between particle radii. We set

$$r = \max(R_i/R_j; R_j/R_i). \tag{10}$$

Dimensionally, a plausible expression of λ is

$$\lambda = c\, h(r) \left(\frac{V_b}{R'}\right)^{1/2}, \tag{11}$$

where c is a constant and h is a function only of r. When introduced in Equations (11) and (9), this form yields a nice fit for the capillary force obtained from direct integration of the Laplace-Young equation by setting $R' = 2R_iR_j/(R_i+R_j)$, $h(r) = r^{-1/2}$ and $c \simeq 0.9$.

Figure 18 shows the plots of Eq. 9 for three different values of the liquid volume V_b and size ratio r together with the corresponding data from direct integration. The forces are normalized by κR and the lengths by λ. The data collapse on the same cruve, indicating again that the force κR and the expression of λ in Eq. (11) characterize correctly the behavior of the capillary bridge.

Finally, the capillary force can be expressed in the following form:

$$f_n^c = \begin{cases} -\kappa\, R & \text{for} \quad \delta_n < 0 \\ -\kappa\, R\, e^{-\delta_n/\lambda} & \text{for} \quad 0 \le \delta_n \le \delta_n^{max} \\ 0 & \text{for} \quad \delta_n > \delta_n^{max} \end{cases}, \tag{12}$$

with

$$\lambda = \frac{c}{\sqrt{2}} \left\{ \frac{1/R_i + 1/R_j}{\max(R_i/R_j; R_j/R_i)} V_b \right\}^{\frac{1}{2}}. \tag{13}$$

In the simulations, the total liquid volume is distributed among all eligible particle pairs (the pairs with a gap below the debonding distance, including the contact points) in proportion to the reduced diameter of each pair. We also assume that the particles are perfectly wettable, i.e. $\theta = 0$. The choice of the liquid volume has no influence on the value of the largest capillary force in the pendular state [43]. For our simulations, we chose a gravimetric water content of 0.007 so that the material is in the pendular state. The coefficient of friction is $\mu = 0.4$ for all simulations.

Distributions of bond forces

We consider force PDF's in a wet packing of 8000 spheres simulated by the MD method for $p_m = 0$ Pa and $p_m = 100$ Pa. The confined sample was obtained by isotropic compaction of a wet packing initially prepared with $p_m = 0$. The packing was then allowed to relax to equilibrium under the action of the applied pressure. This level of confinement is high compared to the reference pressure $p_0 = f_0/\langle d \rangle$ ($p_m/p_0 \simeq 0.5$), yet not too high to mask fully the manifestations of capillary cohesion.

Figure 19 shows the force networks in a narrow slice nearly three particle diameters thick in both samples. The tensile and compressive forces are represented by segments of different colors joining particle centers. As in dry granular media, we observe a highly inhomogeneous distribution both for tensile and compressive forces. The effect of external compressive pressure is to reduce the fraction of tensile bonds. In the unconfined packing, the bond coordination number z (average number of liquid bonds per particle) is $\simeq 6.1$ including nearly 2.97 compressive bonds and 3.13 tensile bonds. As we shall see below, these wet samples involve also a large number of weak forces ($f_n \simeq 0$) corresponding to the contacts where capillary attraction is balanced by elastic repulsion, i.e. $k_n\delta_n + f_0 \simeq 0$.

Figure 20 displays the PDF of normal forces in tensile (negative) and compressive (positive) ranges in the unconfined packing ($p_m = 0$ Pa). We observe two nearly symmetrical parts decaying exponentially from the center:

$$P(f_n) \propto e^{-\alpha_w |f_n|/f_0}, \tag{14}$$

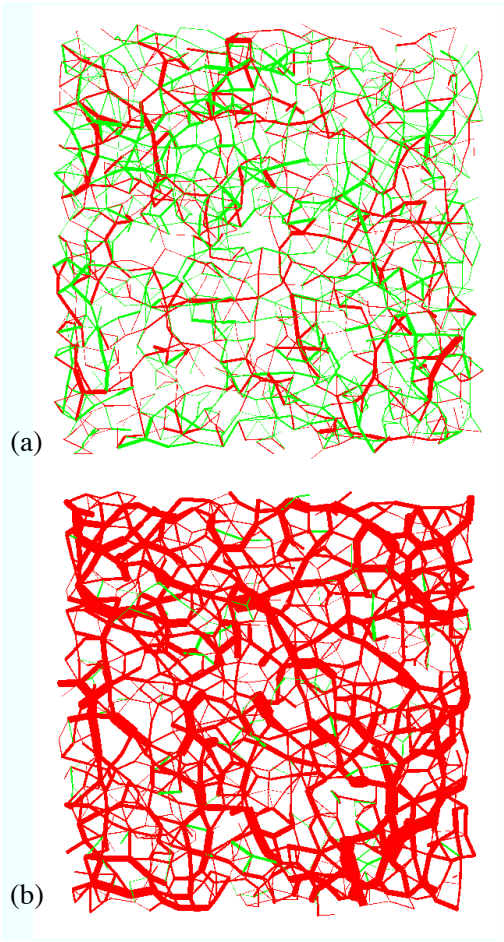

FIGURE 19. Maps of tensile (green) and compressive (red) forces in a thin layer in samples S_6 ($p_m = 0$ Pa) (a) and S_7 ($p_m = 100$ Pa) (b). Line thickness is proportional to the magnitude of the force.

with $\alpha_w \simeq 4$ for both negative and positive forces, and $f_0 = \kappa R_{max}$, where R_{max} is the largest particle radius. In contrast to dry granular media, where the distribution deviates from a purely exponential behavior for weak forces (section), here the exponential behavior extends to the center of the distribution. The tensile range is cut off at $f_n = -f_0$ corresponding to the largest capillary force. Although the confining stress is zero, positive forces as large as $2f_0$ can be found in the system. We also observe in Fig. 20 a distinct peak centered on $f_n = 0$ which is the average force for zero confining pressure. The presence of this peak, resulting from the balance between capillary attraction and elastic repulsion, suggests that a large number of weak forces play a special role with respect to the statics and stability of wet granular materials.

Figure 21 shows the PDF of normal forces in the confined packing. The symmetry of the distribution around $f_n = 0$ is now broken compared to the unconfined case in Fig. 20. The distribution is roughly exponential for both tensile and compressive forces but the exponents are different as in the case of solid cohesion at low matrix volume fraction (section). In the same figure, the PDF of normal forces in a sample without capillary cohesion is shown. We see that the exponent for compressive forces is nearly the same as in the dry packing. Another feature of force distribution observed in Fig. 21 is the presence of a distinct peak centered on zero force which was observed also for the case of unconfined packing in Fig. 20. Hence, this peak reflects a feature of force transmission in wet granular materials that will be analyzed below.

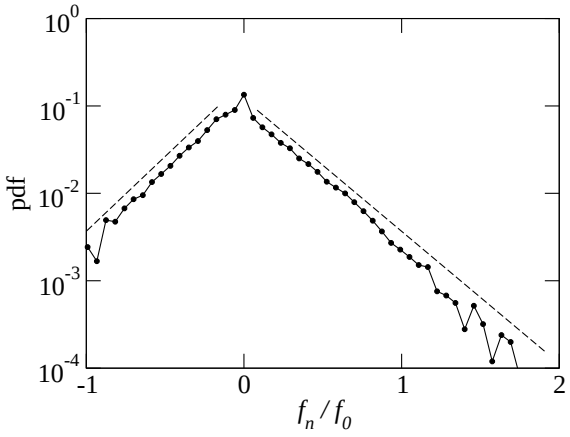

FIGURE 20. Probability density function of normal forces normalized by the largest capillary force f_0 at zero confining pressure.

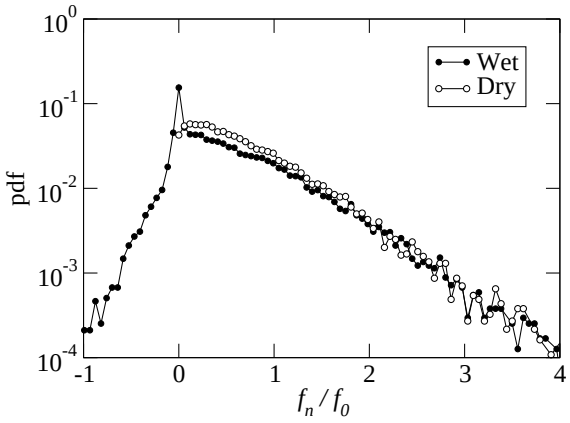

FIGURE 21. Probability density functions of normal forces normalized by the largest capillary force f_0 in the wet and dry confined packings.

Particle pressures

In an unconfined assembly of dry rigid particles, no self-stresses occur and the forces vanish at all contacts. However, the presence of liquid bonds in a wet granular material induces tensile and compressive forces whilst the average force is zero. In other words, the grains keep together to form a self-sustained structure in the absence of confining stresses. In general, various loading histories such as consolidation or differential particle swelling can induce self-stresses in a cohesive packing [44]. In our system, the self-stresses appear during relaxation. This is obviously a consequence of the tensile action of capillary bonds bridging the gaps between neighboring particles within the debonding distance.

For a local description of self-stresses we need to characterize the stress transmission at the particle scale as the smallest scale at which the force balance condition is defined for rigid particles. Although the stress tensor is by definition a macroscopic quantity, it can be shown that an equivalent particle stress σ_i can be defined for each particle i of a granular packing in static equilibrium [33, 45, 46]:

$$(\sigma_i)_{ab} = \frac{1}{V_i} \sum_{j \neq i} f_a^{ij} r_b^{ij}, \tag{15}$$

where r_{ij} is the position of the contact-point of the force f_{ij} of particle j on particle i, and a and b design the Cartesian components. V_i is the free volume of particle i, the sum of the particle volume and a fraction of the pore space:

$$V_i = \frac{\pi d_i^3}{6\nu}, \tag{16}$$

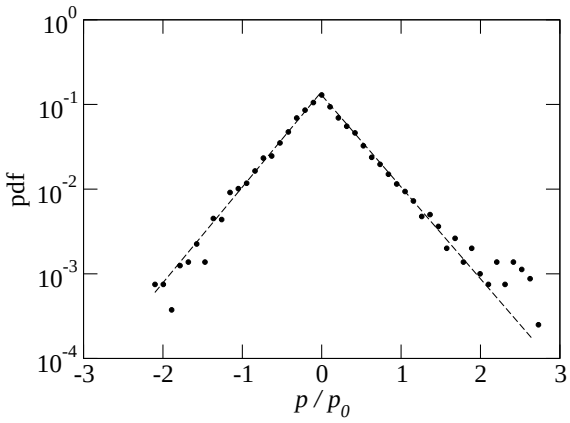

FIGURE 22. Probability density function of particle pressures normalized by reference pressure p_0 (see text) in the unconfined wet packing.

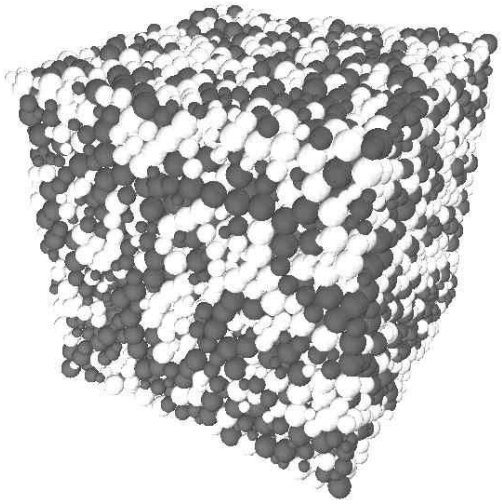

FIGURE 23. The unconfined wet packing with negative (white) and positive (black) particle pressures.

where d_i is the particle diameter, and v is the solid fraction of the packing. The sum of particle stresses σ_i weighted by the corresponding relative free volumes V_i/V tends to the Cauchy stress tensor as the number of particles in a control volume V increases.

From particle stresses we get particle pressures:

$$p_i = \frac{1}{3}\sum_{\alpha=1}^{3}(\sigma_i)_{\alpha\alpha}. \tag{17}$$

Each particle can take on positive or negative pressures according to the forces exerted by neighboring particles. The PDF of particle pressures is displayed in Fig. 22 for the unconfined sample. The pressures have been normalized by a reference pressure $p_0 = f_0/\langle d\rangle^2$. The distribution is symmetric around and peaked on zero pressure, and each part is well fit by an exponential form. This symmetry in the structure of self-stresses must be contrasted with the asymmetric distribution of forces (Fig. 20) due to the cutoff on tensile forces. Obviously, the exponential shape of particle pressure distributions reflects statistically that of bond forces. This distribution extends to the center $p_i = 0$.

Zero particle pressure corresponds to a state where a particle is balanced under the combined action of tensile and compressive forces. Such particle states are not marginal here and they reflect a particular stress transmission in a wet packing. The positive and negative particle pressures form separate phases as observed in Fig. 23 where positive and

negative pressures are represented in black and white, respectively. Each phase percolates throughout the system. The morphology of each phase is approximately filamentary with variable thickness and a large interface between them. A detailed analysis of this structure shows that the particles at the interface between the two phases have a weak pressure and the largest negative or positive pressures are located at the heart of each phase [46].

CONCLUSION

In this paper, the distributions of contact forces and stresses were investigated in cohesive and noncohesive granular media by means of different numerical methods. The exponential fall-off of the number of strong forces and stresses is a robust feature of the distributions in packings of different particle shapes and size distributions with both liquid and solid bonding. In contrast, the force probability density in the range of weak forces and stresses was found to depend on system parameters, taking different shapes from a peaked distribution to a decreasing power law distribution. For wet granular media with a homogeneous distribution of liquid bonds, we showed the nontrivial organization of particle pressures in two separate percolating phases of tensile and compressive particle pressures with an interphase at zero pressure.

For the simulation of solid bonding, we used the lattice element method which provides a suitable framework for the investigation of stress fields in complex granular solids involving a solid matrix sticking to the particles. By coarse-graining the sub-particle stresses, we arrived at the same contact force distributions as in DEM simulations and experiments. Our data are consistent with the fact that the decreasing exponential distribution of strong forces is a signature of *granular disorder*, i.e. the disorder induced by a contiguous network of stiff particles. This signature disappears in the homogeneous limit where there is no stiffness contrast between the particle and matrix phases and the porosity vanishes or when the particles are interposed everywhere by the binding matrix. Our 3D simulations evidence the two limits of homogeneous and granular distributions. For different values of the matrix volume fraction and particle/matrix stiffness ratio, the distributions vary between these two limits.

REFERENCES

1. C. Liu, and H. M. Jaeger, *Phys. Rev. Lett.* **74** (1995).
2. F. Radjai, L. Brendel, and S. Roux, *Phys. Rev. E* **54**, 861 (1996).
3. H. Jaeger, and S. Nagel, *Reviews of Modern Physics* **68**, 1259–1273 (1996).
4. F. Radjai, D. E. Wolf, M. Jean, and J. Moreau, *Phys. Rev. Letter* **80**, 61–64 (1998).
5. D. M. Mueth, H. M. Jaeger, and S. R. Nagel, *Phys. Rev. E* **57**, 3164 (1998).
6. T. S. Majmudar, and R. P. Behringer, *Nature* **435**, 1079–1082 (2005).
7. E. Schlangen, and E. J. Garboczi, *Engineering Fracture Mechanics* **57**, 319–332 (1997).
8. V. Topin, J.-Y. Delenne, F. Radjai, L. Brendel, and F. Mabille, *The European Physical Journal E* **23**, 413–429 (2007).
9. V. Topin, F. Radjai, J.-Y. Delenne, A. Sadoudi, and F. Mabille, *Journal of Cereal Science* **47**, 347–356 (2008).
10. F. Radjai, M. Jean, J.-J. Moreau, and S. Roux, *Phys. Rev. Lett.* **77**, 274– (1996).
11. H. J. Herrmann, and S. Luding, *Continuum Mechanics and Thermodynamics* **10**, 189–231 (1998).
12. G. Lovol, K. Maloy, and E. Flekkoy, *Phys. Rev. E* **60**, 5872–5878 (1999).
13. S. G. Bardenhagen, J. U. Brackbill, and D. Sulsky, *Phys. Rev. E* **62**, 3882–3890 (2000).
14. S. Roux, and F. Radjai, "Statistical approach to the mechanical behavior of granular media," in *Mechanics for a New Millennium*, edited by H. Aref, and J. Philips, Kluwer Acad. Pub., Netherlands, 2001, pp. 181–196.
15. L. E. Silbert, D. Erta, G. S. Grest, T. C. Halsey, and D. Levine, *Phys. Rev. E* **65**, 051307 (2002).
16. P. Dantu, *Ann. Ponts Chauss.* **IV**, 193–202 (1967).
17. A. Drescher, and G. de Josselin de Jong, *J. Mech. Phys. Solids* **20**, 337–351 (1972).
18. F. Radjai and S. Roux, *Phys. Rev. E* **51**, 6177–6187 (1995).
19. F. Radjai, S. Roux, and J. J. Moreau, *Chaos* **9**, 544–550 (1999).
20. S. J. Antony, *Phys Rev E* **63**, 011302 (2001).
21. P. T. Metzger, *Phys. Rev. E* **69**, 053301; discussion 053302 (2004).
22. S. N. Coppersmith, C. Liu, S. Majumdar, O. Narayan, and T. A. Witten, *Phys. Rev. E* **53**, 4673–4685 (1996).
23. P. A. Cundall, and O. D. L. Strack, *Géotechnique* **29**, 47–65 (1979).
24. J. Moreau, *European Journal of Mechanics A/Solids* **supp.**, 93–114 (1994).
25. M. Jean, "The Non Smooth Contact Dynamics method," in *Special issue on modeling contact and friction*, 1999.
26. F. Radjai, and V. Richefeu, *Mechanics of Materials* **41**, 715–728 (2009), ISSN 0167-6636.
27. F. Radjai, I. Preechawuttipong, and R. Peyroux, "Cohesive granular texture," in *Continuous and discontinuous modelling of cohesive frictional materials*, edited by P. Vermeer, S. Diebels, W. Ehlers, H. Herrmann, S. Luding, and E. Ramm, Springer Verlag, Berlin, 2001, pp. 148–159.

28. R. C. Youngquist, P. T. Metzger, and K. N. Kilts, *SIAM J. App. Math.* **65**, 1855 (2005).
29. E. Azéma, G. Saussine, and F. Radjai, *Mechanics of Materials* **41**, 729-741 (2009).
30. E. Azéma, F. Radjai, R. Peyroux, and G. Saussine, *Phys. Rev. E* **76**, 011301 (2007).
31. C. Voivret, F. Radjai, J.-Y. Delenne, and M. S. E. Youssoufi, *Phys. Rev. Lett.* **102**, 178001 (2009).
32. C. Voivret, F. Radjai, J.-Y. Delenne, and M. S. E. Youssoufi, *Phys. Rev. E* **76**, 021301 (2007).
33. J. J. Moreau, "Numerical Investigation of Shear Zones in Granular Materials," in *Friction, Arching, Contact Dynamics*, edited by D. E. Wolf, and P. Grassberger, World Scientific, Singapore, pp. 233–247 (1997).
34. G. Lian, C. Thornton, and M. Adams, *Journal of Colloid and Interface Science* **161**, 138–147 (1993).
35. T. Mikami, H. Kamiya, and M. Horio, *Chemical Engineering Science* **53**, 1927–1940 (1998).
36. F. Soulié, M. S. E. Youssoufi, F. Cherblanc, and C. Saix, *Eur. Phys. J. E* **21**, 349–357 (2006).
37. V. Richefeu, F. Radjai, and M. S. E. Youssoufi, *Eur. Phys. J. E* **21**, 359–369 (2007).
38. C. Willett, M. Adans, S. Johnson, and J. Seville, *Langmuir* **16**, 9396–9405 (2000).
39. L. Bocquet, E. Charlaix, and F. Restagno, *Comptes Rendus Physique* **3**, 207–215 (2002).
40. M. Kohonen, D. Geromichalos, M. Scheel, C. Schier, and S. Herminghaus, *Physica A* **339**, 7–15 (2004).
41. J. N. Israelachvili, *Intermolecular and surface forces*, Academic Press, Cambridge University, 1993.
42. G. Lian, C. Thornton, and M. J. Adams, *Chemical Engineering Science* **53**, 3381–3391 (1998).
43. V. Richefeu, M. S. d El Youssoufi, and F. Radjai, *Phys. Rev. E* **73**, 051304 (2006).
44. M. S. El Youssoufi, J.-Y. Delenne, and F. Radjaï, *Phys. Rev. E* **71**, 051307 (2005).
45. L. Staron, and F. Radjai, *Phys Rev E* **72**, 041308 (2005).
46. V. Richefeu, M. S. El Youssoufi, R. Peyroux, and F. Radjai, *International Journal for Numerical and Analytical Methods in Geomechanics* **32**, 1365–1383 (2008).